Annales Geophysicae (2004) 22: 2805–2817
SRef-ID: 1432-0576/ag/2004-22-2805


Annales Geophysicae

# Observation of $O^+$ ($^4P$-$^4D^0$) lines in electron aurora over Svalbard

**N. Ivchenko[1,2], M. H. Rees[1], B. S. Lanchester[1], D. Lummerzheim[3], M. Galand[4], K. Throp[1], and I. Furniss[5]**

[1]School of Physics and Astronomy, University of Southampton, UK
[2]Alfvén Laboratory, KTH, Stockholm, Sweden
[3]Geophysical Institute, University of Alaska, Fairbanks, USA
[4]Center for Space Physics, Boston University, Boston, Massachusetts, USA
[5]Atmospheric Physics Laboratory, University College London, UK

Received: 12 September 2003 – Revised: 7 May 2004 – Accepted: 12 May 2004 – Published: 7 September 2004

**Abstract.** This work reports on observations of $O^+$ lines in aurora over Svalbard, Norway. The Spectrographic Imaging Facility measures auroral spectra in three wavelength intervals ($H_\beta$, $N_2^+$ 1N(0,2) and $N_2^+$ 1N(1,3)). The oxygen ion $^4P$-$^4D^0$ multiplet (4639–4696 Å) is blended with the $N_2^+$ 1N(1,3) band. It is found that in electron aurora, the brightness of this multiplet, is on average, about 0.1 of the $N_2^+$ 1N(0,2) total brightness. A joint optical and incoherent scatter radar study of an electron aurora event shows that the ratio is enhanced when the ionisation in the upper E-layer (140–190 km) is significant with respect to the E-layer peak below 130 km. Rayed arcs were observed on one such occasion, whereas on other occasions the auroral intensity was below the threshold of the imager. A one-dimensional electron transport model is used to estimate the cross section for production of the multiplet in electron collisions, yielding $0.18\times10^{-18}$ cm$^2$.

**Key words.** Meteorology and atmospheric dynamics (airglow and aurora) – Ionosphere (particle precipitation)

## 1 Introduction

Aurora is produced when atmospheric atoms and molecules excited in collisions with energetic particles (either directly or through a chain of chemical reactions) emit light as they undergo transitions to lower energy states. The auroral spectrum depends on the composition of the upper ionosphere, and the energy distribution functions of the precipitating particles. Understanding the processes shaping the spectrum is important to be able to characterize the auroral precipitation from ground-based spectroscopic observations. While in situ satellite and rocket particle instruments provide an accurate and direct measurement of the energy distribution functions, they suffer from spatial-temporal ambiguity. Information derived from the inversion of auroral emission spectra is coarser and more indirect in nature, but, on the other hand, it records the evolution of the precipitation at one location.

Spectral features originating from various excited states of the atmospheric constituents exhibit different dependences on the precipitation energy spectra. For example, the height-integrated emission rate of $N_2^+$ first negative bands is often treated as proportional to the height-integrated $N_2$ ionization rate and thus proportional to the total energy flux in electron aurora (e.g. Semeter et al., 2001). The forbidden emissions, such as [OI] 5577 and 6300, on the other hand, also depend on the characteristic energy of the accelerated electrons. At lower altitudes, the metastable states are collisionally deactivated, so higher energy electrons, which penetrate deeper in the atmosphere, are less efficient in producing those emissions. Ratios of emissions in different spectral lines have been used to infer the energies of the electrons. Typically, forbidden oxygen emissions are used together with the $N_2^+$ allowed emissions (Vallance Jones et al., 1987) – though their excitation mechanisms are not always easy to understand (Meier et al., 1989). It was also shown that oxygen emissions, which were allowed, are dependent on the energy of the incident electron precipitation (e.g. Lummerzheim, 1987; Lummerzheim et al., 1990).

We present a study of the $O^+$ $^4P$-$^4D^0$ multiplet, observed together with the $N_2^+$ 1N(0,2) and $N_2^+$ 1N(1,3) bands in aurora excited primarily by electron precipitation. This multiplet has long ago been identified (e.g. Chamberlain, 1961; Vallance Jones, 1974), but received little attention. The lines of the multiplet blend with the $N_2^+$ 1N(1,3) band, being of a comparable strength. In studying the $N_2^+$ first negative emissions in twilight conditions resonant scattering of sunlight can be important for low solar depression angles (e.g. Remick et al., 2001). The scattering is most pronounced for bands originating from the ground vibrational state of the $N_2^+$ molecule, and the $N_2^+$ 1N(1,3) band is the brightest of the 1N bands originating from a vibrationally excited state. The intensity ratio of $N_2^+$ 1N(1,3) to $N_2^+$ 1N(0,2) have been studied in relation to the vibrational excitation of $N_2^+$ produced by ionization in proton impact (Vallance and Jones, p. 176, 1974), and the contribution for $O^+$ lines should be properly

*Correspondence to:* N. Ivchenko
(ivchenko@plasma.kth.se)

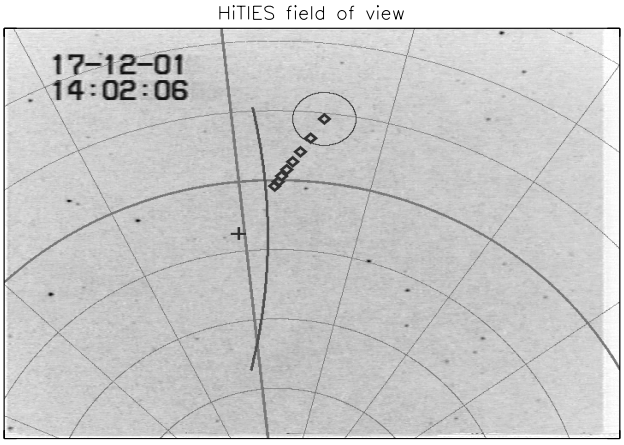


**Fig. 1.** Fields of view of the SIF instruments and the ESR. The cross is the direction of the magnetic zenith. The ESR beam is shown as the circle at 100 km altitude. Diamonds show the centre of the beam at altitudes between 100 km and 240 km with 20 km spacing.

quantified. The companion paper (Ivchenko et al., 2004) studies the mechanisms of the excitation of the $O^+$ lines in proton aurora. Finally, the multiplet feeds the 539 Å UV line, which is relevant for space-borne auroral spectroscopy.

By combining the spectral, imaging and incoherent scatter data, we show that the ratio of the multiplet intensity to the first negative emissions varies in different types of aurora. Enhanced $O^+$ intensities coincide with enhanced ionisation between 140 and 190 km. By inverting the radar electron concentration altitude profiles, the characteristic energy of the precipitation is inferred and related to the ratio of $O^+$ and $N_2^+$ 1N(0,2) brightnesses, which is found to decrease with the electron energy. Assuming a simple functional form for the energy dependence of the cross section, a one-dimensional electron transport model is used to arrive at the absolute value of the cross section for production of the multiplet.

## 2 Instrumentation and Data

### 2.1 Spectrographic Imaging Facility

The Spectrographic Imaging Facility (SIF) is a combination of ground-based optical instruments, jointly operated by the University of Southampton and University College, London. The facility consists of the High Throughput Imaging Echelle Spectrograph (HiTIES), developed at Boston University (Chakrabarti et al., 2001), two photometers and a narrow field ($12\times16°$) auroral imager. SIF is located at the auroral station in the Adventdalen, near Longyearbyen, Svalbard, Norway (78.203° N, 15.829° E). The instruments are co-aligned in the direction of the magnetic zenith. The high-latitude location provides a unique opportunity to study aurora almost 24 h a day during the winter. The location is 7 km north of the EISCAT Svalbard Radar. A comprehensive description of the SIF is provided elsewhere (McWhirter et al., 2003; Lanchester et al., 2003), so only the information essential for this study is given here.

HiTIES is a spectrograph designed specifically for auroral and airglow studies. Light from the slit covering 8° in the sky (see Fig. 1) is collimated, diffracted by echelle grating, and reimaged onto the detector. By using high diffraction orders close to the blaze angle of the grating, high spectral resolution is achieved, together with high throughput. The overlapping diffraction orders are separated by a mosaic of interference filters. The layout of the mosaic determines the spectral and spatial coverage of the instrument. In the data used here, a three-panel mosaic was used, with all the panels extended to cover the whole angular range of 8° centred at the magnetic zenith, while selecting spectral intervals containing the $H_\beta$, $N_2^+$ 1N(0,2) and $N_2^+$ 1N(1,3). The detector used during the winter of 2001/2002 was the Microchannel Intensified CCD (Fordham et al., 1991), on loan from the astronomy group at University College, London. The main advantage of the detector is the photon-counting capability and very low dark count rate and lack of read-out noise.

The spectral resolution of the HiTIES is determined by the width of the slit, which also controls the amount of light entering the instrument. A reasonable compromise in slit width of 0.27 mm (corresponding to about 3 arcminutes on the sky) resulted in a 0.8 Å FWHM instrument function. Typical integration times are between 10 and 60 s. All spectra analyzed in this work are integrated over a 2°-long part of the slit centred at the magnetic zenith.

The Solar Fraunhofer absorption spectrum is used for wavelength calibration of each HiTIES spectral panel. For intensity calibration a "flat field" lamp is used together with the photometers. In 2002/2003 an absolute calibration was carried out with the Tungsten lamp used for calibration of the meridian scanning photometers. The 2001/2002 calibration is referenced to this standard by means of the photometers.

### 2.2 EISCAT Svalbard Radar

Data from the EISCAT Svalbard Radar (ESR) are used here to characterize the electron precipitation. The ESR incoherent scatter radar (Wannberg et al., 1997) measures a number of ionospheric parameters over a range of altitudes. A high frequency signal is transmitted and scattered by electrons in the ionospheric plasma. By analysing the Doppler broadened profiles of the spectrum of the scatter, four parameters can be derived from the data directly: electron number density, plasma velocity, ion and electron temperatures.

### 2.3 Data and analysis

An example of the SIF observation of mixed electron and proton aurora from 16 December 2001 is shown in Fig. 2. Three hours of 30-s integration spectra taken in the direction of the magnetic field are presented. In the top panel, the most prominent features throughout the interval are the $O^+$ lines at 4641.8 Å and 4649.1 Å. Somewhat weaker is the emission between 4652 Å and 4650 Å, corresponding to the blended

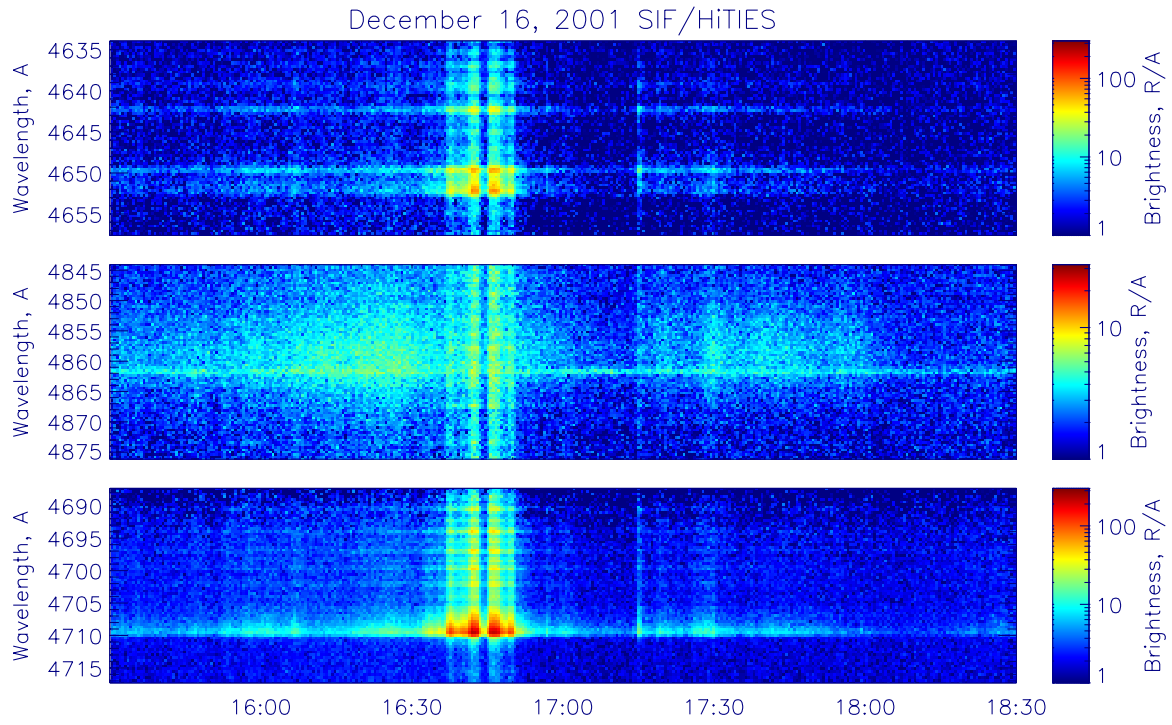


**Fig. 2.** Overview plot of the SIF data from 15:30–18:30 UT, 16 December 2001. The panels show the time dependence of the spectra of the $N_2^+$ 1N(1,3) band, $H_\beta$, and the $N_2^+$ 1N(0,2) band, respectively, as measured by HiTIES.

$N_2^+$ 1N(1,3) emission with the head at 4651.8 Å and another $O^+$ line at 4650.8 Å. Even fainter is the $O^+$ line at 4638.9 Å. At 16:40–16:50 UT there is intense aurora, and the rotational structure of the $N_2^+$ 1N(1,3) band is seen to extend throughout the spectral interval to the blue color of the band's head.

The second panel shows the spectral interval 4843 Å to 4876 Å covering the $H_\beta$ line at 4861 Å. There is weak emission at the unshifted line throughout the interval, most probably coming from the scattering in the geocorona or from a galactic source (see the discussion of $H_\alpha$ emission by Kerr et al., 2001). Doppler shifted and broadened hydrogen emission is seen between 15:30 UT and 17:00 UT, intensifying at 16:30 UT, and later on as weaker and more time varying emissions between 17:15 UT and 18:00 UT.

Structured spectra extending throughout the spectral interval between 16:40–16:50 UT (coincident with the intense emissions in the $N_2^+$ spectral bands) are due to the $N_2$ Vegard-Kaplan (2, 15) band, and are thought to be due to excitation by electrons. While this emission is not the subject of this work, it should be noted in passing that it is a contamination of the $H_\beta$ spectral interval, when studying the $H_\beta$ profiles in proton aurora. However, in most cases the two emissions are easily distinguished visually, so this should not cause any confusion. Besides, our procedure for subtracting the background from the $H_\beta$ profiles (see below) assures that the Vegard-Kaplan bands are not mistaken for the hydrogen emission.

Finally, the bottom panel contains the $N_2^+$ 1N(0,2) band, with its head at 4709.1 Å seen throughout the interval, and the rotational line structure being most clear during the intense burst of the aurora at 16:40–16:50 UT.

To compare the intensities of various spectral features the wavelengths should be known together with the instrument function, integration regions specified and background subtracted. Table 1 presents the wavelengths, transition probabilities and the intensities of single lines relative to the total intensity of the multiplet. The relative intensities are calculated assuming populations of the sublevels of the top state proportional to the statistical weight of the sublevels. The lower $^4P$ state has three sublevels with $j$ of 1/2, 3/2, and 5/2, while the upper $^4D^0$ state has four sublevels with $j$ from 1/2 to 7/2.

The brightnesses of various emissions are extracted from the measured spectra by integrating them over certain wavelength ranges, after having removed the background. Figure 3 presents an example of the real spectrum, with definition of the brightnesses used further in the analysis. In the $N_2^+$ 1N(1,3) panel, covering the wavelengths between 4633.7 Å and 4657.3 Å, the following intervals were selected. The three $O^+$ lines are allocated narrow intervals centred at each line, with integrated brightnesses designated *O1*, *O2*, and *O3*. There is a contribution to these from the $N_2^+$ bands (see below). The head of the $N_2^+$ 1N(1,3) is blended with the 4650.8 Å line of $O^+$, so for the estimate of the intensity of the $N_2^+$ 1N(1,3) band, the interval centred at the maximum intensity is used to obtain *Head(1,3)*.

**Table 1.** Lines of the $O^+$ $^4P$-$^4D^0$ multiplet (NIST Atomic Spectra Database, http://physics.nist.gov/PhysRefData/contents-atomic.html).

| Wavelength, Å | $A_{ki}$, $s^{-1}$ | $J_i - J_k$ | rel. int. |
|---|---|---|---|
| 4638.8558 | 3.61e7 | 1/2–3/2 | 0.069 |
| 4641.8103 | 5.85e7 | 3/2–5/2 | 0.222 |
| 4649.1347 | 7.84e7 | 5/2–7/2 | 0.400 |
| 4650.8384 | 6.70e7 | 1/2–1/2 | 0.084 |
| 4661.6324 | 4.04e7 | 3/2–3/2 | 0.075 |
| 4673.7331 | 1.24e7 | 3/2–1/2 | 0.015 |
| 4676.2350 | 2.05e7 | 5/2–5/2 | 0.077 |
| 4696.3528 | 3.15e7 | 5/2–3/2 | 0.058 |

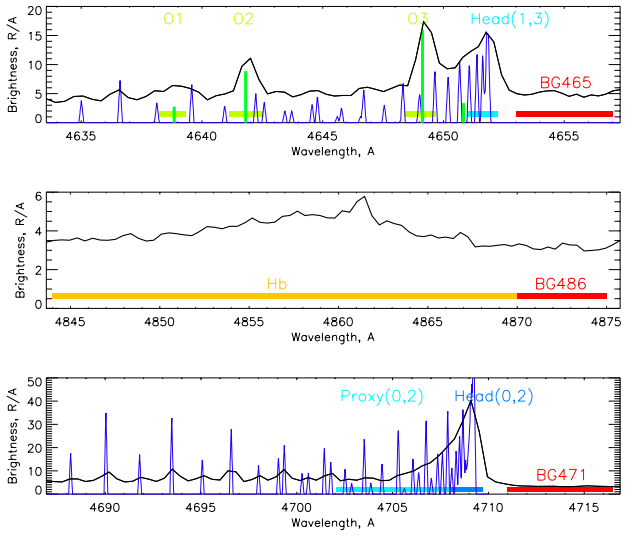


**Fig. 3.** Three-hour integrated spectra of the interval presented in Fig. 2. Overlaid are the synthetic spectra of the $N_2^+$ first negative bands (Degen, 1977) for rotational temperature of 900 K (thin blue line), and the $O^+$ lines (green bars). The horizontal bars designate the spectral intervals used to derive the intensities of the emissions – see text.

Integrated intensity *BG465* is a measure of background brightness. In the $H_\beta$ panel, two brightnesses are calculated: Hb, integrated over the Doppler profile of the hydrogen line, and *BG486* – an estimate of the background. Both electron and proton precipitation were observed during the integration period of the spectrum, and it shows both the $H_\beta$ profile, peaking at about 4858 Å, and the Vegard-Kaplan band, excited mostly in bright electron aurora, visible as rotational lines peaking at 4848.5 Å, 4850.5 Å, 4852.5 Å, 4855 Å, etc. The rotational structure of the band extends throughout the interval, and contributes to the *BG486* brightness as well. In the first approximation, the contribution is constant over the whole spectral interval, which makes the Hb after subtraction of the background effectively insensitive to the VK bands, and characteristic of the proton precipitation. Finally, in the $N_2^+$ 1N(0,2) panel, three brightnesses are calculated:

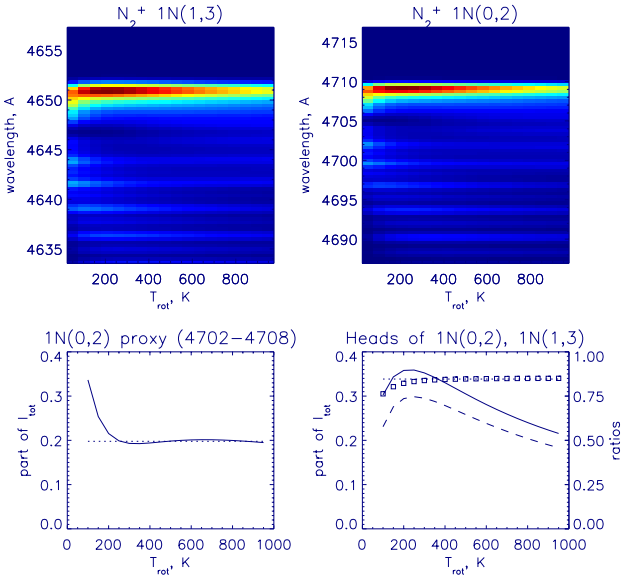


**Fig. 4.** Top: rotational structure of 1N(1,3) and 1N(0,2) bands, synthetic spectra are convolved with the instrument function for various rotational temperatures of the parent $N_2$. Bottom left – the brightness of *Proxy(0,2)* relative to the total $N_2^+$ 1N(0,2) band brightness as a function of the rotational temperature. Bottom right – brightnesses of the *Head(0,2)* (solid line) and *Head(1,3)* (dashed line) relative to the total brightness of the respective band, as a function of the rotational temperature. Squares show the ratio of the dashed curve to the solid (axis on the right).

the background *BG471*, the head of the band *Head(0,2)* and a broader interval around the band origin *Proxy(0,2)*.

The spectra of the $N_2^+$ depend on the rotational temperature of the parent $N_2$. To estimate the contribution of the emissions to the selected brightness intervals, synthetic spectra for a range of rotation temperatures were convolved with the instrument function. The upper panels in Fig. 4 present rotational development of $N_2^+$ 1N(0,2) and $N_2^+$ 1N(1,3) as a function of rotational temperature. The heads of the bands are the most prominent features of the spectra, and those least dependent on the background. However, the portion of the total band brightness contained in its head decreases with increasing rotational temperature (see lower right panel).

With the chosen definition of the band head intervals (see Fig. 3), their ratio is independent of the rotational temperature, above 200 K, and is 0.84 (marked with a dotted horizontal line in Fig. 4). This means that the ratio of the band brightnesses can be calculated from the ratio of *Head(1,3)* and *Head(0,2)*, when accounting for this factor. It is possible to choose a spectral interval in such a way that its brightness is proportional to the total brightness of the band within a range of temperatures. The brightness of the *Proxy(0,2)* interval chosen, as shown in Fig. 3, is 0.198 of the total brightness of $N_2^+$ 1N(0,2). This relation holds to within 3% for temperatures over 250 K (see lower left panel). This allows one to estimate the total brightness of the $N_2^+$ 1N(0,2) band from *Proxy(0,2)*. The *Head(1,3)* is contaminated by the 4650.8 Å

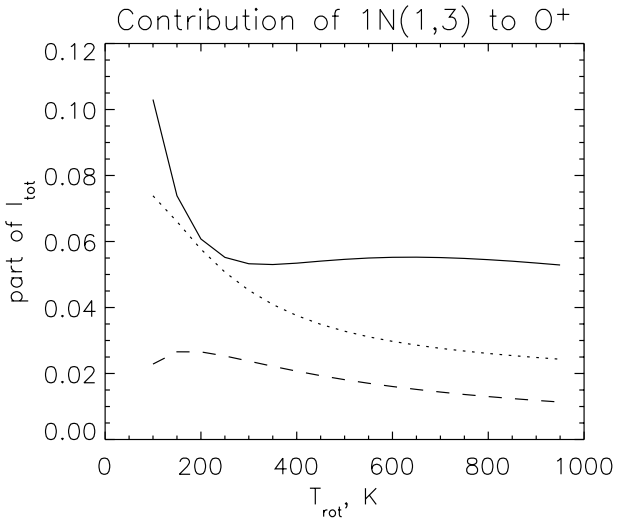


**Fig. 5.** Relative contribution of $N_2^+$ 1N(1,3) intensity contributing to the *O1* (dashes), *O2* (dots), and *O3* (solid) spectral intervals, vs. the rotational temperature.

$O^+$ line. A careful examination of the $O^+$ spectra convolved with the instrument function shows that 3.1% of the total $O^+$ multiplet brightness adds to the *Head(1,3)* brightness, which is subtracted easily.

In the same way, the relative contribution of $N_2^+$ 1N(1,3) to the interval used for deriving the $O^+$ line brightnesses may be estimated. Figure 5 shows these relative contributions as a function of the rotational temperature. The average values of 0.020, 0.035, and 0.055 were used for subtraction from the *O1*, *O2*, and *O3* brightnesses, respectively. Also, we calculate the relative contribution of the $O^+$ multiplet to the *O1*, *O2*, and *O3* brightnesses. Assuming the relative brightnesses of individual lines, as given in Table 1, and convolving those with the instrument function, the relative contributions of the total brightness are 0.057, 0.0207 and 0.357 for *O1*, *O2*, and *O3*, respectively (some of the line brightness "leaks" outside the intervals). In Sect. 3 we confirm that the relative intensities of the oxygen lines are not inconsistent with the assumption. However, the *O3* spectral interval contains the strongest multiplet line, and least contamination from other (weaker) oxygen and nitrogen lines, and is the best candidate for estimating the intensity of the multiplet as the whole.

The background brightness, as estimated from *BG465*, is often higher than that estimated from the *BG486* and *BG471*, with the two latter brightnesses agreeing very well between themselves (assuming a constant spectral brightness). This is due to the presence of additional unresolved emissions between 4650Å and 4700Å. These emissions have been attributed to the $N_2$ 2P(0,5) and $N_2$ 2P(4,10) bands, as well as the $N_2$ VK(4,16) band (Sivjee, 1980). From our observations, the intensity of these emissions seems to be only weakly related to the presence of the aurora, and they sometimes dominate the spectrum when little $N_2^+$ 1N(0,2) and $N_2^+$ 1N(1,3) are present. The spectrum from one such occasion,

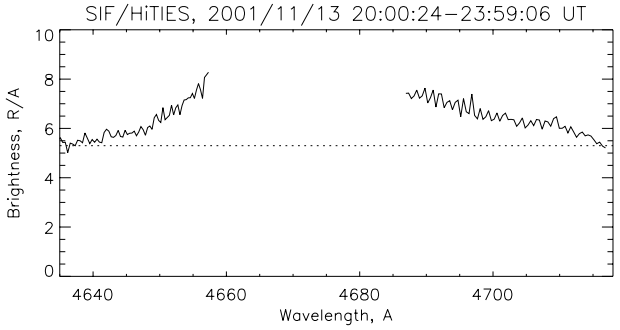


**Fig. 6.** Night-sky spectrum devoid of aurora on 13 November 2001, showing the background emissions in the $N_2^+$ 1N(0,2) and $N_2^+$ 1N(1,3) panels.

on 13 November 2001, is shown in Fig. 6. Assuming the flat continuum over the whole interval region, the spectral shape can be used to subtract the contribution of these emissions from both $N_2^+$ 1N(0,2) and $N_2^+$ 1N(1,3) panels. The intensities of these contaminating emissions are estimated from the difference between *BG465* and *BG471*.

## 3 Statistical relations between brightnesses

During two intervals (17 December 2001, 12:30–16:30 UT, and 14 January 2002, 18:30–20:30 UT) the intensity of Doppler shifted $H_\beta$ emission was well below the intensity of the unshifted line, indicating that the aurora was excited by electron precipitation. These intervals are studied to establish a statistical relation between the $N_2^+$ and $O^+$ emission brightnesses.

Figure 7 presents a scatter plot of the brightnesses of the $O^+$ multiplet (derived from the *O3* brightness, characterizing the strongest line of the multiplet) vs. the intensity of the $N_2^+$ 1N(0,2) band (further denoted *I(0,2)*) derived from the *Proxy(0,2)*. There is considerable scatter in the plot, with the linear fit yielding $I(O^+)$=3.1 R + 0.091 *I(0,2)*, with a correlation coefficient of 0.65 for *I(0,2)* brightnesses below 400 R, and $I(O^+)$=12.0 R+0.064 *I(0,2)* with a correlation coefficient of 0.73 for *I(0,2)*>400 R. The fact that the ratio of the $O^+$ multiplet to the $N_2^+$ 1N(0,2) decreases with auroral brightness is probably due to the fact that there is a correlation between the characteristic energy and the total energy flux in the precipitating electrons (Christensen et al., 1987), brighter aurora being on average produced by more energetic electrons.

A useful diagnostic of the data is to look at the relation between the intensities of $N_2^+$ 1N(0,2) and $N_2^+$ 1N(1,3) bands. Theory predicts that for parent $N_2$ temperatures typical for the ionosphere, the distribution of $N_2^+$ ions produced in electron collisions is given by the Franck-Condon factors for the ground vibrational state of the $N_2$ molecule, and the relative intensities of the bands originating from the same upper vibration state are determined by appropriate

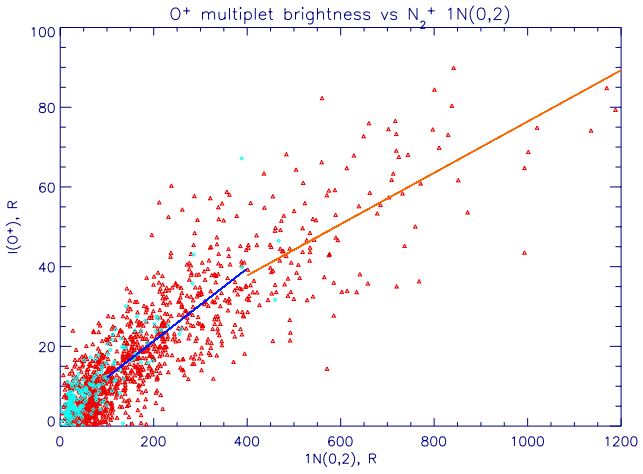


**Fig. 7.** Plot of I($O^+$) vs. $N_2^+$ 1N(0,2) in electron aurora. The brightnesses are derived as I($O^+$)=O3/0.357 and *I(0,2)=Proxy(0,2)/0.198*. Red triangles – 17 December 2001 points, cyan diamonds – 14 January 2002 points. Solid lines show two linear fits to the data: blue for intensities of $N_2^+$ 1N(0,2) between 100 R and 400 R, orange – for intensities above 400 R.

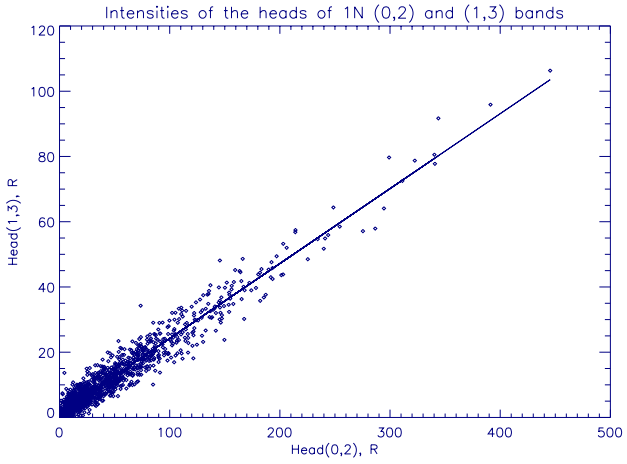


**Fig. 8.** Plot of *Head(1,3)* vs. *Head(0,2)* in electron aurora.

Einstein coefficients. Based on these calculations, the ratio of *I(1,3)/I(0,2)* should be 0.222. A scatter plot of the *Head(1,3)* vs. the intensity of the *Head(0,2)* is shown in Fig. 8. The linear fit to the data is *Head(1,3)*=1.24 *R*+0.23 *Head(0,2)*, with a correlation coefficient of 0.967. Taking into consideration that the two heads as defined here contain different portions of the band brightnesses (see Fig. 4), and neglecting the offset, the ratio of the total band intensities becomes *I(1,3)/I(0,2)*=(*Head(1,3)*/0.84)/*Head(0,2)*=0.27. Though this is 20% higher than predicted by theory, this may be considered a good agreement. There are several possible sources of the discrepancy: the experimental errors, including the calibration and background subtraction, additional emissions in the spectral interval used for estimating *Head(1,3)*, non-thermal vibrational excitation of the parent

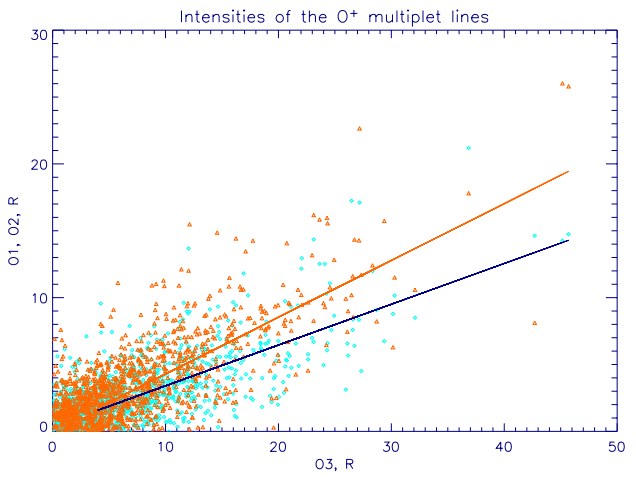


**Fig. 9.** Plots of *O1* vs. *O3* (cyan diamonds), and *O2* vs. *O3* (orange triangles) in electron aurora. Solid lines show linear fits to the data.

$N_2$, and finally, the deviation of the vibrational development from the Franck-Condon factors.

The relative intensities of the oxygen lines are also in reasonable agreement with our assumption of equal probability of the upper sublevel population. Figure 9 shows the scatter plots of *O1* and *O2* brigtnesses vs. *O3*. The linear fits yield *O1*=0.35 R+0.30 *O3* and *O2*=0.04 R+0.42 *O3* with correlations of 0.66 and 0.70, respectively. The expected values from convolving lines with the instrument function and integrating over the intervals used for these lines, are 0.17 and 0.56, respectively (see Sect. 2.3). The *O1* brightness is almost twice the expected value, which is probably due to contamination of the spectral interval by other oxygen and nitrogen emissions. The *O2* brightness is 25% below the expected value which is acceptable, taking into account the noise level.

### 3.1 14 January 2002 event

On 14 January 2002 the spectrograph was operated in 30-s integration mode between 18:30 UT and 20:30 UT. The ESR was running the TAU0 modulation experiment, which utilizes two alternating code signals, allowing for complete coverage from the E-layer to topside at a time resolution of 6.4 s. The 42-m dish is fixed and aligned in the magnetic zenith, as are the SIF instruments. To improve the signal-to-noise ratio and facilitate the comparisons, 32-s time integration was applied to the radar data prior to the analysis. An aurora of moderate intensity developed in the field of view of the SIF and ESR, allowing for a detailed study of the oxygen emission and its relationship to local ionisation.

Figure 10 presents an overview of the event. The ESR observed enhancements of the E-layer electron number density (top panel), indicative of auroral precipitation – at 18:43 UT, 18:46 UT, 18:53 UT, a weaker one between 18:57 UT and 19:07 UT, at 19:12 UT, 19:14 UT and 19:18 UT, 19:28 UT to 19:36 UT, and around 20:00 UT. These were accompanied by the brightenings of $N_2^+$ and $O^+$ emissions (third and

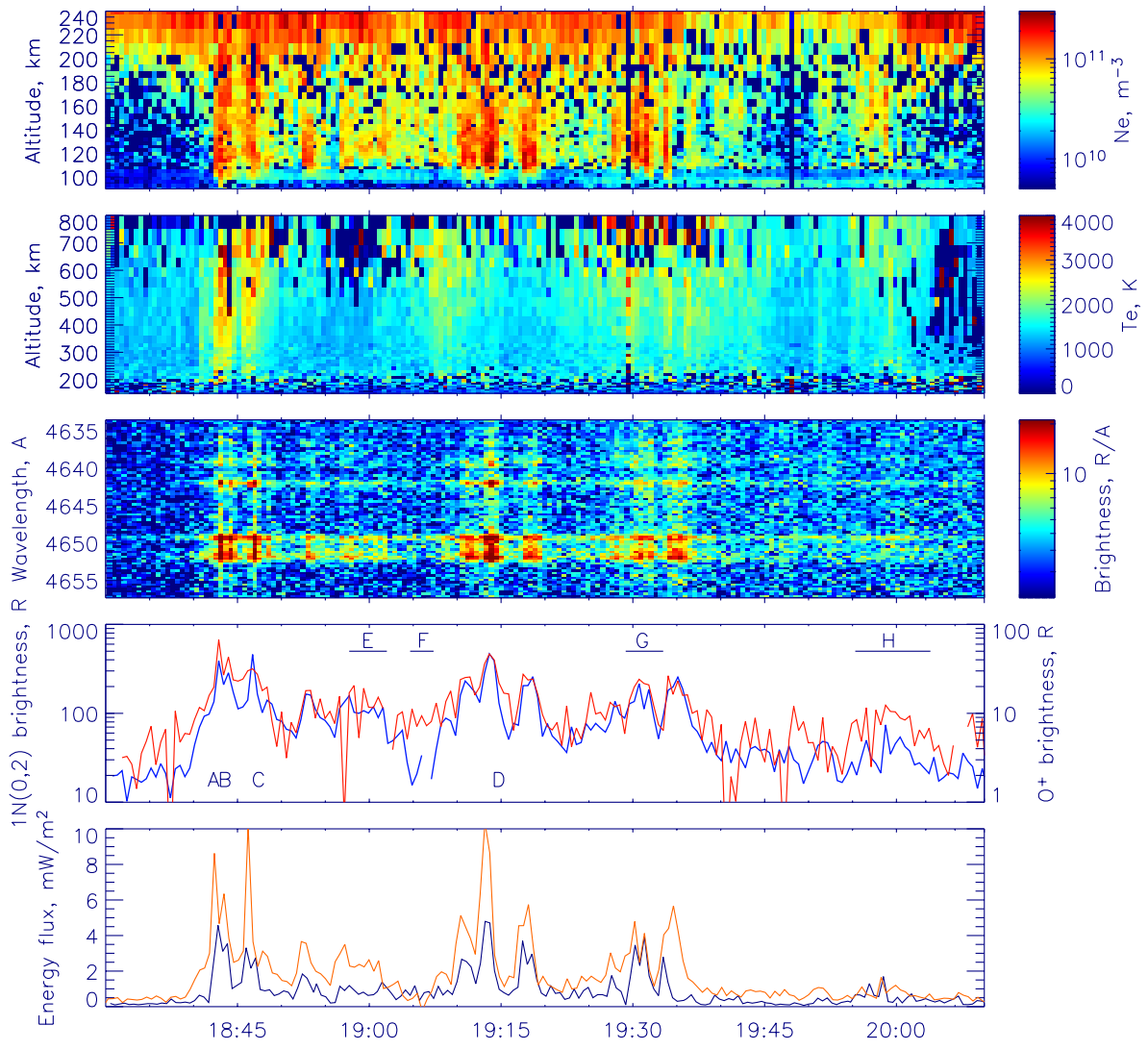


**Fig. 10.** The event of 14 January 2002. Panels from top to bottom: ESR measurement of electron number density in the E-layer, and electron temperature in the F-layer; time evolution of 1N(1,3) spectra recorded by the HiTIES; line plots of $N_2^+$ 1N(0,2) (blue) and $O^+$ multiplet (red) intensities; precipitating electron energy flux derived from the radar measurements (blue) and from the optical data (orange). See text.

fourth panels), showing a one-to-one correspondence. In the bottom panel, the energy flux of the precipitating electrons derived from the ESR ionization profiles (see below) is compared with the energy flux determined from $N_2^+$ 1N(0,2) emission (using a conversion factor of 45 R per 1 mW/m$^2$, derived from our model – see below). Even though the instruments are 7 km apart, which means that the magnetic zenith of the SIF does not coincide with that of the ESR, the qualitative agreement of the curves warrants the further consideration of the data. For integration times of 30 s, as used here, fast motions of the aurora in most cases provide the spatial averaging to make the comparison valid.

The brightnesses of the oxygen ion multiplet, and the nitrogen first negative emissions follow each other rather closely when the latter are scaled with the factor of 0.1, as found above (note the different scale for the $O^+$ brightness in panel 4). However, a closer look at the data reveals several regions where the proportionality is not observed. Between 18:35 UT and 18:48 UT the $O^+$ lines are relatively stronger (apart from one point at 18:47 UT where strong $N_2^+$ 1N(0,2) is observed), as they are between 19:04 UT and 19:08 UT, and 19:47 UT to 20:10 UT. Several representative intervals were selected for joint analysis of the data. Where aurora is sufficiently intense (intervals A, B, C, and D) single integration periods of the spectrograph and radar data are put in the context of the imager data. For intervals E, F, G and H the precipitation was less intense, rendering the imager data less useful. For these intervals several electron number density profiles and HiTIES spectra had to be integrated. The results of the analysis of all these intervals, as described in detail below, are summarized in Table 2.

**Table 2.** Summary of the intervals on 14 January 2002: characteristic energy of the best fits for maxwellian and monoenergetic input electron spectra, quality of the fit, observed ratio of $O^+{}^4P$-$^4D^0$ multiplet intensity to the $N_2^+$ 1N(0,2) intensity, modeled brightness from the $O_2$ dissociative ionisation/excitation, difference between the observed $O^+$ brightness and $O_2 + e$ contribution, modeled brightness from O+$e$ assuming maximum cross section of $0.18\times10^{-18}$ cm$^2$.

| | A | B | C | D | E | F | G | H |
|---|---|---|---|---|---|---|---|---|
| $E_{maxw}$, keV | 0.50 | 0.97 | 0.80 | 0.88 | 0.50 | 0.50 | 0.73 | 0.50 |
| $E_{mono}$, keV | 1.07 | 2.78 | 2.53 | 3.06 | 1.90 | 1.07 | 2.30 | 1.07 |
| Fit | fair | fair | fair | good | poor | fair | good | poor |
| I($O^+$)/1N(0,2), $\times100$ | 14.62 | 17.32 | 6.90 | 10.23 | 12.55 | 12.61 | 12.6 | 22.54 |
| $I_{mod}(O_2\rightarrow O^+)$/1N(0,2), $\times100$ | 1.92 | 2.42 | | 2.34 | | 1.92 | 2.17 | |
| I($O\rightarrow O^+$)/1N(0,2), $\times100$ | 12.7 | 14.9 | | 7.89 | | 10.7 | 10.43 | |
| $I_{mod}(O\rightarrow O^+)$/1N(0,2), $\times100$ | 11.4 | 7.9 | | 8.2 | | 11.4 | 9.2 | |

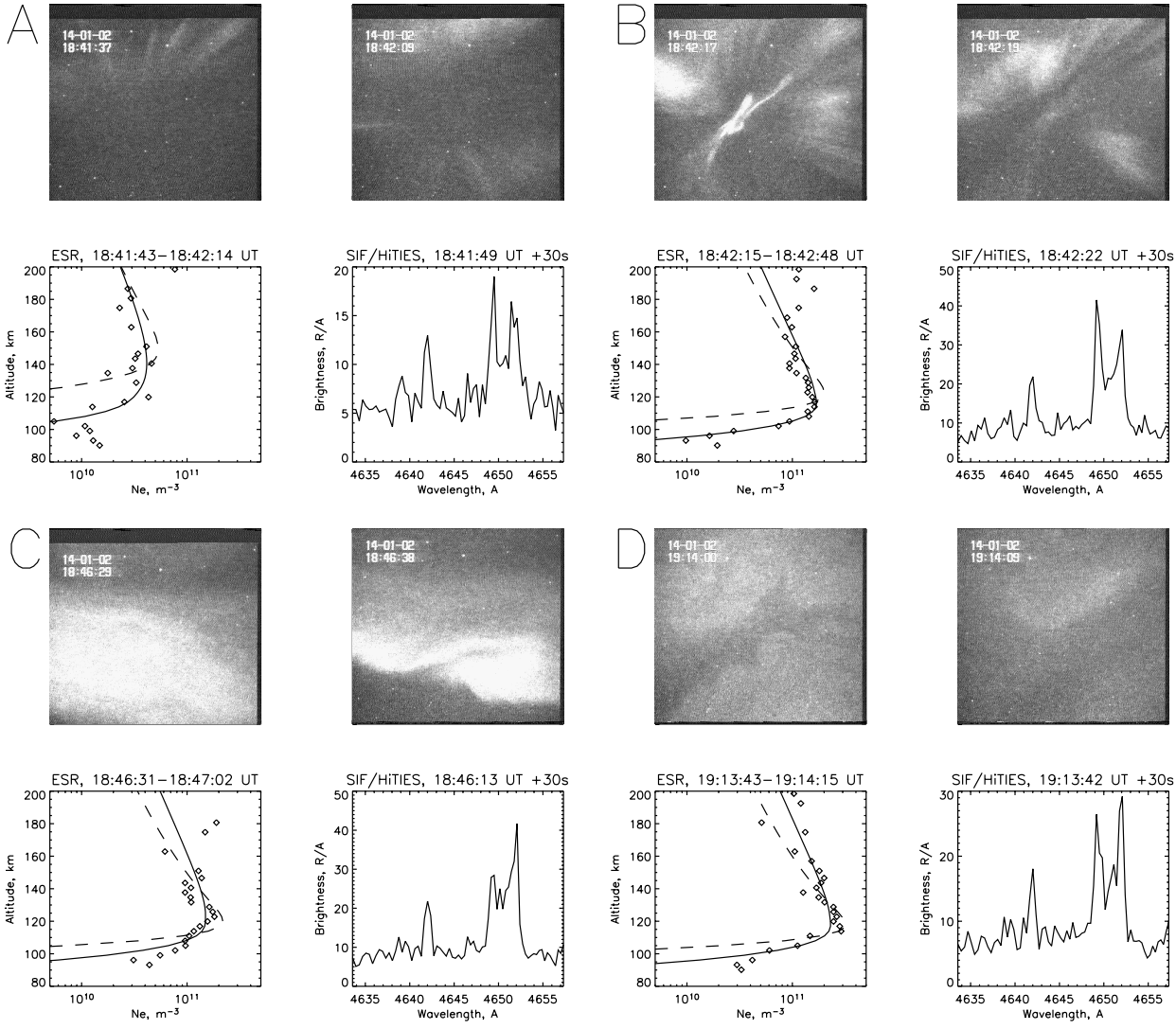


**Fig. 11.** Snapshots of four intervals on 14 January 2002. For each of the intervals two images from the SIF narrow field imager are given, the ESR electron number density altitude profile, and the HiTIES spectrum of the $N_2^+$ 1N(1,3) wavelength interval. Solid lines in the density profiles show a fit with the maxwellian precipitation, and dashed lines – monoenergetic precipitation. See text.

An inversion procedure developed by Palmer (1995) was applied to the E-layer electron number density profiles to infer the characteristics of the electron precipitation. The density profiles below 180 km were converted to altitude ionisation profiles, assuming ionisation-recombination equilibrium with a recombination rate of $2\times10^{-7}\,\mathrm{cm^{-3}\,s^{-1}}$. These ionisation profiles were then fitted with a pre-calculated library of ionisation profiles produced by electron precipitation with monoenergetic or maxwellian distribution functions. The best fits for both kinds of spectrum are recorded, given by the energy flux and characteristic energy of the precipitation. This simple and relatively coarse method has been shown to produce reliable results (Lanchester et al., 1998). The fit for the energy flux will be an underestimate in time-varying aurora for two reasons. The integration of the radar spectra over a time interval is linear in density (which is given by the power of the scatter in the first approximation), whereas the energy flux is given by the square of the equilibrium density. Also, the assumption of ionisation-recombination equilibrium itself breaks down at short time-scales compared with the recombination time scale, which varies between under a second below 100 km and tens of seconds in the upper E-layer and lower F-layer. The fitted value for the characteristic energy, on the other hand, depends mostly on the shape of the profiles, and thus is less affected by the time variations in the characteristic energy of the precipitation.

Figure 11 presents data from single ESR and SIF measurements, together with representative camera images from within the integration periods. Interval A, centred around 18:42:00 UT, is in the beginning of a period of bright aurora in the field of view of the SIF. The activity starts as a rayed arc comes from the south (top of the camera images) at around 18:41:30 UT. Rays and structured rayed arcs appear throughout the field of view, moving and changing intensity rapidly. During this interval the radar recorded densities ranging between $1\times10^{10}\,\mathrm{m^{-3}}$ and $4\times10^{10}\,\mathrm{m^{-3}}$ at altitudes between 100 km and 180 km. The best fits have characteristic energies of 1.07 keV (monoenergetic electrons) and 0.5 keV (maxwellian distribution) respectively. Both fits predict more pronounced peaks of the ionisation than those observed, with maxwellian precipitation being probably closer to reality. In the $N_2^+$ 1N(1,3) panel the oxygen line at 4649.13 Å is the brightest feature (when considering spectral brightness).

The next sample of both instruments is selected as interval B. The rays intensify, and are observed as coronal structure as they fill the entire field of view of the camera. In the magnetic zenith a very narrow structure transverse to the magnetic field is present. The ESR electron densities are now over $1\times10^{11}\,\mathrm{m^{-3}}$ for most of the altitude range between 100 km and 180 km. As in the previous interval, the fall-off of the electron density with altitude is rather slow, even though there is a more pronounced peak at about 115 km. The maxwellian fit with the characteristic energy of 0.97 keV is again closer to the data than the monoenergetic with 2.78 keV energy, both falling short of the measured electron concentrations above 150 km. The $N_2^+$ 1N(1,3) panel spectrum shows strong oxygen lines, at higher intensities.

Interval C is the only point between 18:30 UT and 18:48 UT where the ratio of the I($O^+$)/I(1N(0,2)) is clearly below 0.1. The imager recorded a band of intense aurora developing folds in the field of view. The band stayed to the north of the magnetic zenith, occasionally reaching the field of view of the spectrograph, but not that of the ESR. This must be the explanation for the relatively low (for such a bright aurora) electron densities – ranging between $1\times10^{11}\,\mathrm{m^{-3}}$ and $2.5\times10^{11}\,\mathrm{m^{-3}}$. While the fits to the ESR electron density profiles show reasonable agreement with the measurements, they cannot be directly compared to the Hi-TIES spectrum, which shows a dominating peak of the $N_2^+$ 1N(1,3) band.

Interval D is chosen as a brightest point within the auroral event observed between 19:10 UT and 19:20 UT. Throughout the event the intensities of the $O^+$ lines and the $N_2^+$ 1N(0,2) are related by the factor of 0.1. The imager observed "diffuse" aurora covering much of the field of view, with dark structures appearing inside it. The appearance of the aurora is clearly distinctive from the rays characteristic of intervals A and B. The ionisation profile produced by the maxwellian distribution of electrons with characteristic energy of 0.88 keV is in good agreement with the observed density profile, while the monoenergetic (3.06 keV) profile underestimates the density both below and above the peak, which itself is reproduced somewhat better.

Figure 12 shows the ESR density profiles for intervals E, F, G, and H, together with the monoenergetic and maxwellian ionisation profiles. In cases F and H the $O^+$ lines are well above the average of 0.1 of the $N_2^+$ 1N(0,2) brightness, and the both density profiles lack a clear E-region peak. The monoenergetic profiles fail to reproduce the density distribution, while the maxwellian ones are closer to the observation, but still predict an ionisation peak between 120 and 140 km. Profile E (with a ratio of $O^+$ multiplet to $N_2^+$ 1N(0,2) brightness close to 0.1) shows both a peak at just above 120 km, and a flat profile above the peak, which results in a rather poor fit for both the maxwellian and the monoenergetic distributions. Finally, case G corresponds to an interval where the $O^+$ lines are only slightly above the average 0.1 of the $N_2^+$ 1N(0,2) intensity, and the ionisation profiles corresponds well to a maxwellian precipitation with characteristic energy of 0.73 keV.

The second panel in Fig. 10 shows the F-layer electron temperature. There are several enhancements of the electron temperature, the most pronounced one being related to the interval 18:40 UT to 18:50 UT, when rayed arcs were observed (intervals A, B and C). In contrast to this, interval D does not show any significant enhancements in $T_e$, even though the electron concentration produced in the E-layer is even higher than for the former intervals.

### 3.2 Estimation of the excitation cross sections

To study the excitation of the $^4P$-$^4D^0$ multiplet we use an electron transport model, together with a model cross section energy dependence. By comparing the predicted

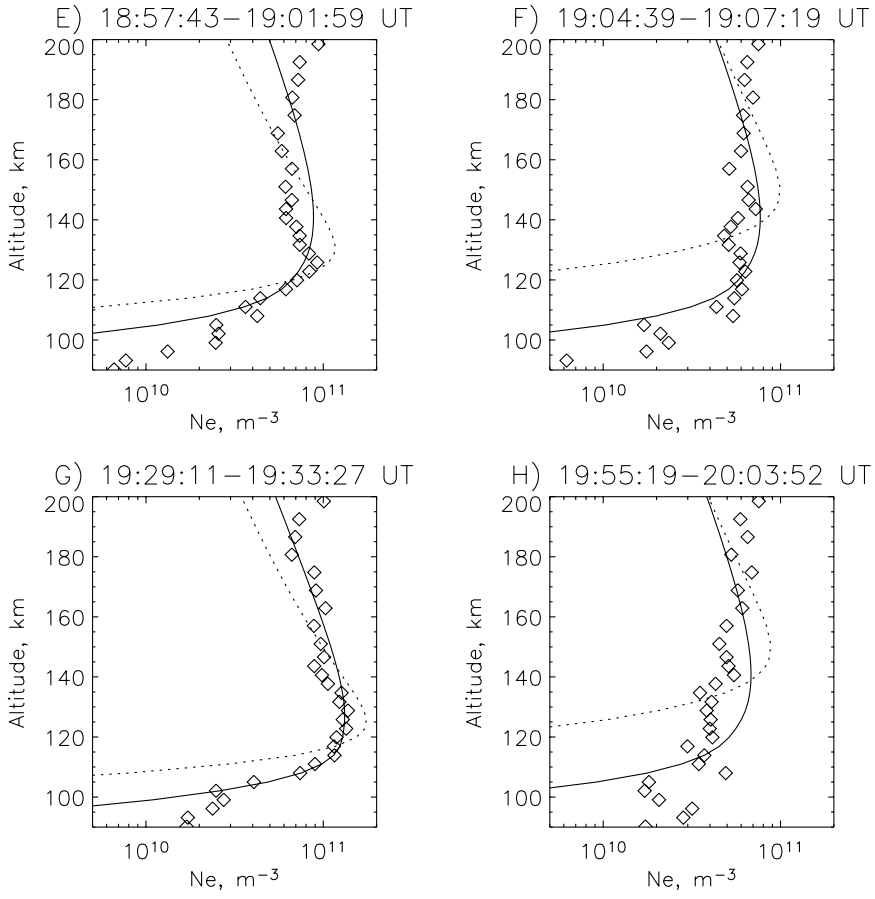


**Fig. 12.** ESR density profiles and SIF spectra for intervals E, F, G and H in Fig. 10.

$I(O^+)/I(0,2)$ ratios for maxwellian input spectra with characteristic energies obtained from the fits (see Table 2) to observed ratios, the absolute scale can be put on the cross section.

The excitation energy of the $O^+$ $^4D^0$ state is 25.66 eV. The abundance of ionized oxygen is several orders of magnitude below that of the neutrals in the altitude range where the auroral emissions can be produced (80–500 km), so excitation of $O^+$ will make a negligible contribution to the production of the multiplet. Thus, the viable processes for production of the lines are the ionization-excitation with the threshold of 39.27 eV:

$$O + e \rightarrow O^+(^4D^0) + e_{sec} + e, \quad (1)$$

and the dissociative ionization of $O_2$ with the threshold of 44.39 eV

$$O_2 + e \rightarrow O^+(^4D^0) + O + e_{sec} + e. \quad (2)$$

To the best of our knowledge, no measurements or theoretical calculations provide the differential cross section for reaction (1). For the allowed transitions the electron impact excitation cross sections behave asymptotically at high energies as $E^{-1}\ln E$, exhibiting a maximum at 4–5 threshold energies (Vallance Jones, 1974). We assume a model cross section in the functional form of

$$\sigma(E) \propto (1 - e^{-0.3\frac{E-E_0}{E_0}})E^{-1}\ln E, \quad (3)$$

corresponding to maximum cross section at 160 eV (see Fig. 13).

The cross section for reaction (2) has been measured by Schulman et al. (1985) as a by-product of their work on the neutral oxygen atom emissions produced in electron impact dissociative ionization of $O_2$. It was found that the cross section for the two $3s^4P_{1/2,5/2}-3p^4D^0_{1/2,7/2}$ lines at 4650 Å has a maximum at 200 eV, where its value is $0.17\times10^{-18}$ cm$^2$. These two lines amount to 0.484 of the total brightness of the multiplet.

The above cross sections were used, together with an electron transport model for the ionosphere (Lummerzheim and Lilensten, 1994), to estimate the brightnesses of the produced emissions. To obtain a quantitative scale on the cross section, a series of model runs was made for the cases where the best fit to the electron density profiles was achieved (cases A, B, D, F and G). Maxwellian distributions with corresponding characteristic energies were used as input at 500 km with a 1 mW/m$^2$ energy flux. The model calculated the magnetic zenith brightness of the $N_2^+$ 1N(0,2) band, assuming the

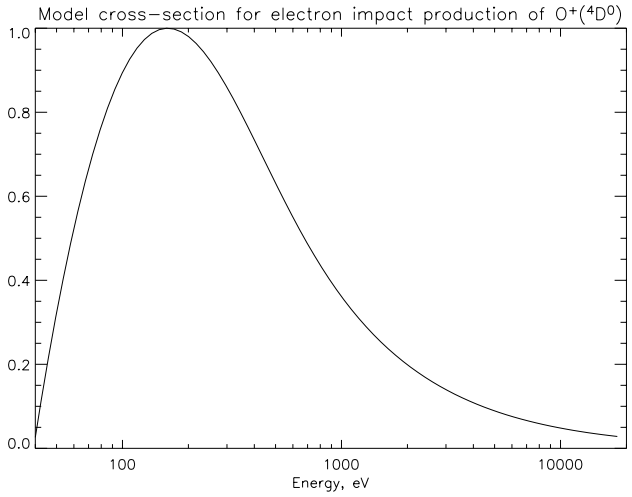


**Fig. 13.** Model shape of the cross section for production of the $O^+$ $^4D^0$ state from atomic oxygen.

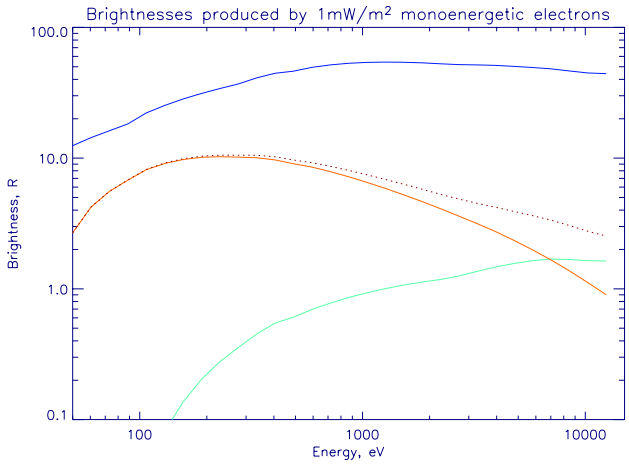


**Fig. 14.** Height-integrated emission rate of $N_2^+$ 1N(0,2) band (blue curve) and $O^+$ multiplet vs. the energy of monoenergetic electron precipitation. Green curve shows the intensity due to the dissociative ionisation, red curve shows the intensity due to the direct ionisation of O (using the cross section estimated in this work). The dotted line is the total $O^+$ multiplet intensity.

branching ratio of 0.145 for production of $N_2^+$(B) state (van Zyl and Pendleton, 1995), and using the value of 0.04 for the ratio of $N_2^+$ 1N(0,2) to the total first negative system intensity (Vallance Jones, 1974). Also, the brightness of the $O^+$ multiplet produced in (2) was calculated, and that directly excited in (1). The ratios of the $O^+$ brightnesses were compared to the observed ratio in the selected cases. Comparing the observed brightnesses with the predicted ones indicates that the excitation in the dissociative ionisation contributes to a small portion of the total multiplet brightness (see the fourth row in Table 2), the bulk of the emissions coming from the direct process. The second row from the bottom in Table 2 shows the observed value of the brightness produced in the direct O+*e* processes, which was obtained as the difference of the observed $I(O+)/I\,(0,2)$ and the modelled contribution from $O_2$ dissociative ionization. Scaling the model cross section shape to the maximum value of $0.18\times10^{-18}$ cm$^2$ results in the best fit between the modelled (last row) and the observed value of the brightness excited in the ionisation of atomic O.

Using this cross section, the energy dependence of the $O^+$ line emission rate was studied. A number of runs were made for monoenergetic electrons with the energy flux at 500 km of 1 mW/m$^2$. Figure 14 shows the calculated height-integrated emission rates of the $O^+$ multiplet produced in the ionization excitation of O, due to dissociative ionization of molecular oxygen, as well as the $N_2^+$ 1N(0,2). The oxygen multiplet is most sensitive to the low energy precipitation, producing maximum brightness at 200 eV. At low energies the dissociative ionisation is negligible, but becomes comparable to the direct ionisation of atomic oxygen at energies of about 7 keV.

## 4 Discussion

The 14 January 2002 event contained several instances of electron precipitation with varying characteristics in the field of view of the instruments. The ratio of the intensities of the $O^+$ multiplet to the $N_2^+$ band emission appears to be strongly related to the type of auroral forms in the field of view of the optical instruments, which is borne out by the variable height profiles of electron concentration measured by the radar, and by the occurrence of raised electron temperatures in structured rayed aurora. We have used these differences to investigate the mechanisms for production of the O+ multiplet and to estimate the cross section for one of the production mechanisms.

The intensity ratio of the $N_2^+$ 1N(1,3) and $N_2^+$ 1N(0,2) bands is somewhat larger than that predicted from Franck-Condon factors. Also, the brightness of the 4638.9 Å and 4641.8 Å lines relative to the 4649.1 Å line are somewhat different than those assuming equal probability excitation of the states. In both cases the discrepancies can probably be accounted for by the measurement errors and other contaminating emissions, which become more important for relatively weaker spectral features. Quite noticeable is the difference between the energy flux derived from the radar ionisation profiles, and the $N_2^+$ 1N(0,2) brightness. The energy flux derived from the first negative band brightness exceeds that from the radar measurements by a factor of 2 to 3. This is the case even though the atmospheric extinction of the emission has not been taken into account. This could have decreased the observed intensities by a factor of 1.5 (Lummerzheim et al., 1990). A similar discrepancy was noted by Vallance Jones et al. (1987), who attributed it to the cumulative result of small errors in calibrations, recombination coefficient used and cross sections employed in the model. Another possibility, which should be pointed out, is that the nature of the time and space integration is different for optical and radar measurements. Whereas the optical emissions intensity is proportional to the energy flux of

the precipitation, the equilibrium ionospheric density is proportional to the square root of the energy flux. So, unless the precipitation is constant in time for the whole integration period and in space across the whole field of view of the radar, the radar estimate will be an underestimate of the energy flux. The situation is similar to that discussed by Semeter and Doe (2002) encountered in interpreting the ionospheric conductance derived from global auroral images.

The observed enhancement of the $O^+$ lines is associated with ionisation in the upper E-layer. In most of the analyzed profiles from the 14 January 2001 event, the Maxwellian precipitating electron spectra fitted the data better than the monoenergetic beam. This is not the case generally, and Strickland et al. (1994) present examples of both types of profiles. They attribute the maxwellian spectra to the diffuse aurora. In our case, the intervals A and B are associated with the highly structured rayed arcs and enhanced electron temperature in the topside F-layer. Such arcs, observed as coronal structures in the images, are reported to be associated with coherent radar spectra (Sedgemore-Schulthess et al., 1999), which are often interpreted in terms of current instabilities. High field-aligned current densities were reported by Lanchester et al. (2001) from analysis of highly enhanced electron temperature in a structured aurora, and by satellite measurements (e.g. Ivchenko and Marklund, 2002). Such high current densities are most probably transient and are related to Alfvénic structures associated with the aurora (Stasiewicz et al., 2000). Dispersive Alfvén waves are related to suprathermal electron bursts – field-aligned population extending up to 1 keV energies (e.g. Andersson et al., 2002). Such precipitation should be effective in exciting F-region auroras (Chaston et al., 2003).

A major uncertainty in the derivation of the emission cross section by comparison of the model with the observations lies in the altitude profiles of the neutral constituents. Particularly, the concentration of atomic oxygen at high latitudes may differ from the MSIS90 model (used in the electron transport code) by a factor of up to 2 (Lummerzheim et al., 1990; Shepherd et al., 1995; Nicholas et al., 1997), which is attributed to the effects of the aurora itself (Christensen et al., 1997).

Few studies have been made into the cross sections of $O^+$ emissions, which could be related to auroral and airglow studies. Apart from the cited paper by Schulman et al. (1985) mentioning the cross section of the $^4P$-$^4D^0$ multiplet, the only other paper we are aware of is that by Haasz and deLeeuw (1976). They measured effective emissions cross sections of $O^+$ lines at 4350 Å and 4416 Å. For the excitation of these two multiplets from the electron collisions with neutral oxygen atoms, the values of $2.3\times10^{-20}$ cm$^2$ and $5.9\times10^{-20}$ cm$^2$, respectively, were obtained; for the dissociative ionisation-excitation of $O_2$, the values were $1.45\times10^{-20}$ cm$^2$ and $1.40\times10^{-20}$ cm$^2$, respectively. However, their cross sections were obtained for the energy range of 0.6 to 3.0 keV, and thus cannot be directly compared to our result. It should also be pointed out that our results, as well as those by Haasz and deLeeuw (1976) and Schulman et al. (1985), refer to emission cross sections, including cascading from higher lying states, possibly excited by electron impact.

## 5 Conclusions

1. The $^4P$-$^4D^0$ multiplet of ionized oxygen is persistently present in the electron aurora. Its intensity amounts, on average, to 0.1 of $N_2^+$ 1N(0,2) intensity.

2. The $O^+$ lines are relatively brighter in low characteristic energy electron precipitation, which is in agreement with electron transport model calculations.

3. Comparison of the observations with a model shape of the differential cross section yields a peak cross section of $0.18\times10^{-18}$ cm$^2$ for the assumed functional form of the energy dependence. The main source of uncertainty is associated with using the MSIS90 atomic oxygen concentrations, which may disagree with the actual concentrations in the auroral zone.

4. Rayed arcs are observed to be associated with enhanced $O^+$ line brightnesses, and E-layer density profiles that decrease slowly with altitude. Also, enhanced F-layer electron temperature is associated with the interval when the rayed arcs are observed.

5. The observed ratios between the brightnesses of $N_2^+$ 1N(1,3) and $N_2^+$ 1N(0,2) bands are about 20% higher than those predicted by the Franck-Condon factors, which should not be taken as a discrepancy, considering that various theoretical predictions differ between themselves.

*Acknowledgements.* NI is supported by a grant from PPARC in the UK. MG is supported by NASA grant NAG5-12773. The EISCAT Scientific Association is supported by Centre National de la Recherche Scientifique of France, Max-Planck-Gesellschaft of Germany, Particle Physics and Astronomy Research Council of the United Kingdom, Norges Forskningsråd of Norway, Naturvetenskapliga Forskningsådet of Sweden, Suomen Akatemia of Finland and the National Institute of Polar Research of Japan.

Topical Editor M. Lester thanks C. Deehr and K. Kaila for their help in evaluating this paper.

## References

Andersson, L., Ivchenko, N., Clemmons, J., Namgaladze, A. A., Gustavsson, B., Wahlund, J.-E., Eliasson, L., and Yurik, R. Y.: Electron signatures and Alfvén waves, J. Geophys. Res., 107, 15–1, 2002.

Chakrabarti, S., Pallamraju, D., Baumgardner, J., and Vaillancourt, J.: HiTIES: A high throughput imaging echelle spectrograph for ground-based visible airglow and auroral studies, J. Geophys. Res., 106, 30 337–30 348, 2001.

Chamberlain, J. W.: Physics of the Aurora and Airglow, Academic Press, New York and London, 1961.

Chaston, C. C., Peticolas, L. M., Bonnell, J. W., Carlson, C. W., Ergun, R. E., McFadden, J. P., and Strangeway, R. J.: Width and brightness of auroral arcs driven by inertial Alfven waves, J. Geophys. Res., 17–1, 2003.

Christensen, A. B., Lyons, L. R., Hecht, J. H., Sivjee, G. G., and Meier, R. R.: Magnetic field-aligned electric field acceleration and the characteristics of the optical aurora, J. Geophys. Res., 92, 6163–6167, 1987.

Christensen, A. B., Hecht, J. H., Walterscheid, R. L., Larsen, M. F., and Sharp, W. E.: Depletion of oxygen in aurora: Evidence for a local mechanism, J. Geophys. Res., 102, 22 273–22 277, 1997.

Degen, V.: Modeling of N2/+/ first negative spectra excited by electron impact on N2, J. of Quant. Spectr. and Rad. Trans., 18, 113–119, 1977.

Fordham, J. L., Bellis, J. G., Bone, D. A., and Norton, T. J.: MIC photon counting detector, in: Proc. SPIE, Vol. 1449, Electron Image Tubes and Image Intensifiers II, edited by Csorba, I. P., 87–98, 1991.

Haasz, A. A. and deLeeuw, J. H.: Effective electron impact excitation cross sections for N2, O2, and O1, J. Geophys. Res., 81, 4031–4034, 1976.

Ivchenko, N. and Marklund, G.: "Current singularities" observed on Astrid-2, Adv. Space Rec., 30, 1779–1782, 2002.

Ivchenko, N., Galand, M., Lanchester, B. S., Rees, M. H., Lummerzheim, D., Furniss, I., and Fordham, J.: Observations of $O^+$ ($^4P$-$^4D^0$) lines in proton aurora over Svalbard, Geophys. Res. Lett., doi:10.1029/2003GL019313, 31, 2004.

Kerr, R. B., Garcia, R., He, X., Noto, J., Lancaster, R. S., Tepley, C. A., González, S. A., Friedman, J., Doe, R. A., Lappen, M., and McCormack, B.: Periodic variations of geocoronal Balmer-alpha brightness due to solar-driven exospheric abundance variations, J. Geophys. Res., 106, 28 797–28 818, 2001.

Lanchester, B. S., Rees, M. H., Sedgemore, K. J. F., Palmer, J. R., Frey, H. U., and Kaila, K. U.: Ionospheric response to variable electric fields in small-scale auroral structures, Ann. Geophys., 16, 1343–1354, 1998.

Lanchester, B. S., Rees, M. H., Lummerzheim, D., Otto, A., Sedgemore-Schulthess, K. J. F., Zhu, H., and McCrea, I. W.: Ohmic heating as evidence for strong field-aligned currents in filamentary aurora, J. Geophys. Res., 106, 1785–1794, 2001.

Lanchester, B. S., Rees, M. H., Robertson, S. C., Lummerzheim, D., Galand, M., Mendillo, M., Baumgardner, J., Furniss, I., and Aylward, A. D.: Proton and electron precipitation over Svalbard – first results from a new Imaging Spectrograph (HiTIES), Proc. of Atmospheric Studies by Optical Methods, Sodankylä Geophys. Obs. Pub. 92, 33–36, 2003.

Lummerzheim, D.: Electron Transport and Optical Emissions in the Aurora., Ph.D. Thesis, 1987.

Lummerzheim, D. and Lilensten, J.: Electron transport and energy degradation in the ionosphere: Evaluation of the numerical solution, comparison with laboratory experiments and auroral observations, Ann. Geophys., 12, 1039–1051, 1994.

Lummerzheim, D., Rees, M. H., and Romick, G. J.: The application of spectroscopic studies of the aurora to thermospheric neutral composition, Planet. Space Sci., 38, 67–78, 1990.

McWhirter, I., Furniss, I., Lanchester, B. S., Robertson, S. C., Baumgardner, J., and Mendillo, M.: A new spectrograph platform for auroral studies in Svalbard, Proc. of Atmospheric Studies by Optical Methods, Sodankylä Geophys. Obs. Pub. 92, 73–76, 2003.

Meier, R. R., Strickland, D. J., Hecht, J. H., and Christensen, A. B.: Deducing composition and incident electron spectra from ground-based auroral optical measurements: A study of auroral red line processes, J. Geophys. Res., 94, 13 541–13 552, 1989.

Nicholas, A. C., Craven, J. D., and Frank, L. A.: A survey of large-scale variations in thermospheric oxygen column density with magnetic activity as inferred from observations of the FUV dayglow, J. Geophys. Res., 102, 4493–4510, 1997.

Palmer, J.: Plasma Density Variations in the Aurora, Ph.D. Thesis, 1995.

Remick, K. J., Smith, R. W., and Lummerzheim, D.: The significance of resonant scatter in the measurement of $N_2^+$ first negative 0-1 emissions during auroral activity, J. Atmos. Terr. Phys., 63, 295–308, 2001.

Schulman, M. B., Sharpton, F. A., Chung, S., Lin, C. C., and Anderson, L. W.: Emission from oxygen atoms produced by electron-impact dissociative excitation of oxygen molecules, Phys. Rev. A, 32, 2100–2116, 1985.

Sedgemore-Schulthess, K. J. F., Lockwood, M., Trondsen, T. S., Lanchester, B. S., Rees, M. H., Lorentzen, D. A., and Moen, J.: Coherent EISCAT Svalbard Radar spectra from the dayside cusp/cleft and their implications for transient field-aligned currents, J. Geophys. Res., 104, 24 613–24 624, 1999.

Semeter, J. and Doe, R.: On the proper interpretation of ionospheric conductance estimated through satellite photometry, J. Geophys. Res., pp. 19–1, 2002.

Semeter, J., Lummerzheim, D., and Haerendel, G.: Simultaneous multispectral imaging of the discrete aurora, J. Atmos. Solar-Terr. Phys., 63, 1981–1992, 2001.

Shepherd, M. G., McConnell, J. C., Tobiska, W. K., Gladstone, G. R., Chakrabarti, S., and Schmidtke, G.: Inference of atomic oxygen concentration from remote sensing of optical aurora, J. Geophys. Res., 100, 17 415–17 428, 1995.

Sivjee, G. G.: Anomalous vibrational distribution of N2/+/1 NG emissions from a proton aurora, J. Geophys. Res., 85, 206–212, 1980.

Stasiewicz, K., Bellan, P., Chaston, C., Kletzing, C., Lysak, R., Maggs, J., Pokhotelov, O., Seyler, C., Shukla, P., Stenflo, L., Streltsov, A., and Wahlund, J.-E.: Small Scale Alfvénic Structure in the Aurora, Space Sci. Rev., 92, 423–533, 2000.

Strickland, D. J., Hecht, J. H., Christensen, A. B., and Kelly, J.: Relationship between energy flux Q and mean energy (mean value of E) of auroral electron spectra based on radar data from the 1987 CEDAR Campaign at Sondre Stromfjord, Greenland, J. Geophys. Res., 99, 19 467–19 473, 1994.

Vallance Jones, A.: Aurora, D. Reidel Publishing Company, Dordrecht, Holland, 1974.

Vallance Jones, A., Gattinger, R. L., Shih, P., Meriwether, J. W., and Wickwar, V. B.: Optical and radar characterization of a short-lived auroral event at high latitude, J. Geophys. Res., 92, 4575–4589, 1987.

van Zyl, B. and Pendleton, W.: $N_2^+$(X), $N_2^+$(A), and $N_2^+$(B) production in $e^-$+$N_2$ collisions, J. Geophys. Res., 100, 23 755–23 762, 1995.

Wannberg, G., Wolf, I., Vanhainen, L.-G., Koskenniemi, K., Röttger, J., Postila, M., Markkanen, J., Jacobsen, R., Stenberg, A., Larsen, R., Eliassen, S., Heck, S., and Huuskonen, A.: The EISCAT Svalbard radar: A case study in modern incoherent scatter radar system design, Radio Science, 32, 2283–2307, 1997.